Volume 12
Number 4
28 January 2024
Pages 833–1116

Journal of Materials Chemistry B

Materials for biology and medicine

rsc.li/materials-b

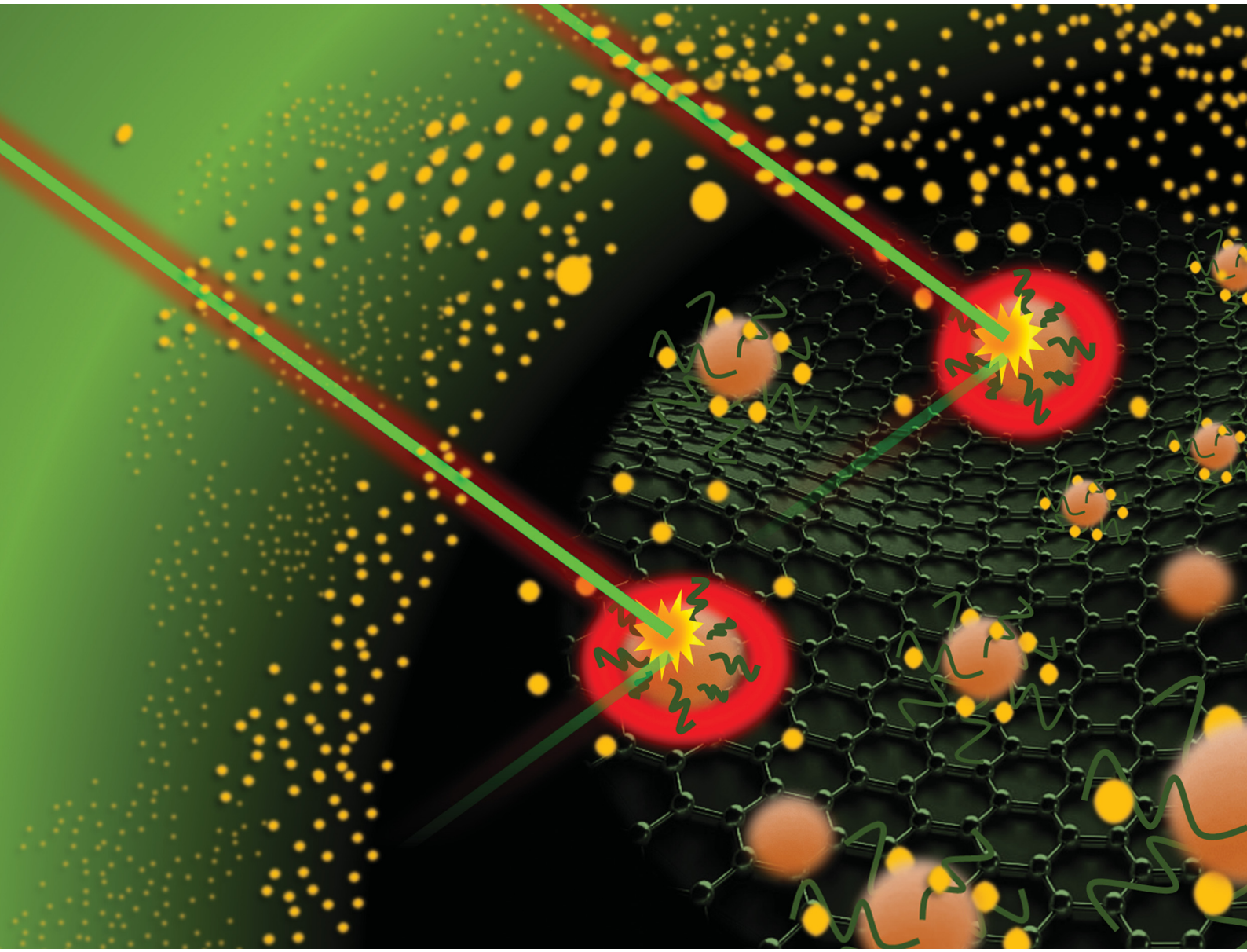

ISSN 2050-750X

ROYAL SOCIETY OF CHEMISTRY

PAPER

Salvatore Petralia *et al.*

Red light-triggerable nanohybrids of graphene oxide, gold nanoparticles and thermo-responsive polymers for combined photothermia and drug release effects

Journal of Materials Chemistry B

ROYAL SOCIETY OF CHEMISTRY

PAPER

View Article Online
View Journal | View Issue

Cite this: J. Mater. Chem. B, 2024, 12, 952

Red light-triggerable nanohybrids of graphene oxide, gold nanoparticles and thermo-responsive polymers for combined photothermia and drug release effects†

Grazia M. L. Consoli,[ab] Ludovica Maugeri,[c] Giuseppe Forte,[c] Gianpiero Buscarino,[d] Antonino Gulino,[e] Luca Lanzanò,[f] Paolo Bonacci,[g] Nicolò Musso[g] and Salvatore Petralia *[abch]

The development of multifunctional nanohybrid systems for combined photo-induced hyperthermia and drug release is a challenging topic in the research of advanced materials for application in the biomedical field. Here, we report the first example of a three-component red-light-responsive nanosystem consisting of graphene oxide, gold nanoparticles and poly-*N*-isopropylacrylamide (GO–Au–PNM). The GO–Au–PNM nanostructures were characterized by spectroscopic techniques and atomic force microscopy. They exhibited photothermal conversion effects at various wavelengths, lower critical solution temperature (LCST) behaviour, and curcumin (Curc) loading capacity. The formation of GO–Au–PNM/Curc adducts and photothermally controlled drug release, triggered by red-light excitation (680 nm), were demonstrated using spectroscopic techniques. Drug–polymer interaction and drug–release mechanism were well supported by modelling simulation calculations. The cellular uptake of GO–Au–PNM/Curc was imaged by confocal laser scanning microscopy. *In vitro* experiments revealed the excellent biocompatibility of the GO–Au–PNM that did not affect the viability of human cells.

Received 16th August 2023,
Accepted 8th November 2023

DOI: 10.1039/d3tb01863f

rsc.li/materials-b

Introduction

A nanohybrid system in the nanoscale dimension implies the combination of a variety of organic, inorganic, or bioactive components in a single material with either enhanced or entirely new properties.[1] This approach has provided the opportunity to create a huge number of novel materials with well-defined structures and functions.[2–4] Combining exclusive features such as optical, electrical and photo-responsive properties, a nanohybrid system offers advantages in different application fields including biomedical, coating, energy storage, catalysis, and sensing.[5–7] In the biomedical field, light-responsive photothermal systems, that allow for a controlled release of drugs in specific regions, are appealing for more effective and safer therapy. Indeed, photothermia and drug release restricted to irradiated areas can reduce the dosage and side effects of conventional chemotherapy. In this scenario, nanohybrid systems that combine the photothermal properties of metal nanoparticles (NPs) and graphene oxide (GO)-based nanostructures and the thermo-responsive properties of poly-(*N*-isopropylacrylamide) (PNM) are attracting interest. GO nanosheets have a large surface area and can load nanostructures as support materials. In particular, the oxygenated functional groups of GO can be utilized as nucleation centres to grow or anchor NPs. PNM is a polymer largely investigated for biomedical applications because of its low toxicity, chemical stability, temperature- and pH-responsivity.[4] The stimuli-responsivity of the PNM has been exploited to develop temperature-responsive drug delivery systems. It has been reported that at temperatures below the lower critical solution temperature (LCST), PNM adopts a hydrophilic coil-extended-conformation stabilized by favourable interactions with water molecules. Instead, at a

[a] CNR-Institute of Biomolecular Chemistry, Via Paolo Gaifami 18, 95126 Catania, Italy. E-mail: salvatore.petralia@unict.it
[b] CIB-Interuniversity Consortium for Biotechnologies U.O. of Catania, Via Flavia, 23/1, 34148 Trieste, Italy
[c] Department of Drug and Health Sciences, University of Catania, Via Santa Sofia 64, 95125 Catania, Italy
[d] Department of Physics and Chemistry, University of Palermo, Via Archirafi 36, Palermo, Italy
[e] Department of Chemical Science, University of Catania, and I.N.S.T.M. UdR of Catania, Via Santa Sofia 64, 95125 Catania, Italy
[f] Department of Physics and Astronomy "Ettore Majorana", University of Catania, Via S. Sofia 64, 95123 Catania, Italy
[g] Department of Biomedical and Biotechnological Sciences, University of Catania, Via S. Sofia 97, Catania, Italy
[h] NANOMED, Research Centre for Nanomedicine and Pharmaceutical Nanotechnology, University of Catania, Viale A. Doria 6, 95124 Catania, Italy

† Electronic supplementary information (ESI) available. See DOI: https://doi.org/10.1039/d3tb01863f

temperature above the LCST value (typically 33–35 °C), a transition takes place, and the polymer adopts a hydrophobic globule-like conformation. In this collapsed state, water molecules are expelled from the shell and the amount of hydrogen bonds decreases allowing the release of entrapped drug molecules. Curcumin (Cur) is a natural substance with a wide range of biological properties[8,9] and biomedical applications.[10] Cur has shown anticancer,[11] antimicrobial,[12] antioxidant and anti-inflammatory,[13] antidiabetic,[14] hepato-[15] and neuro-protective activity.[16] However, poor stability, water solubility, and bioavailability have limited the clinical use of curcumin and stimulated intense research aimed at overcoming these issues through entrapment in nanocarriers.[17–20] Since hyperthermia enhances the anticancer activity of Cur,[21] photothermal nanosystems are interesting Cur delivery systems.[22]

Two-component nanohybrid composites that integrate the properties of GO with nanoparticles or organic molecules were widely reported in the literature[23,24] and investigated for different applications including drug delivery,[25] NO photo-release,[26] and antibacterial[27] activity. Differently, very few examples of three-component GO-based nanosystems are present in the literature.[28]

In this work, we report the first example of a three-component nanosystem in which GO sheets are decorated with photothermal gold nanoparticles (AuNPs), which are further functionalized with the thermo-responsive PNM polymer. For application as a light-actuated device for remote controlled drug release, Cur was entrapped into the GO–Au–PNM nanocontainer (Scheme 1A). Cur was selected as a hydrophobic drug model whose performance can be improved by entrapment in a photothermal drug delivery system for dual chemo-photothermal therapy outcomes. The PNM covalently linked to the AuNP surface was chosen to induce a red shift of the localized surface plasmon resonance (LSPR) band to higher wavelengths. Consequently, more biocompatible light could trigger the photothermal-induced PNM conformational change and promote the release of Cur from the nanosystem. The morphology, spectroscopic properties and photothermal behaviour of the hybrid nanosystem as well as the red light-triggered hyperthermia and hyperthermia-induced drug release were investigated (Scheme 1B).

Results and discussion

Design, synthesis, and characterization of the GO–Au–PNM nanosystem

Nanohybrid systems composed of photothermal materials and thermo-responsive polymers are fascinating stimuli-responsive drug delivery systems widely developed by our group.[29–32] They match dark stability, good biocompatibility, and absorption in the visible and near-infrared (NIR) region suitable to effectively promote the photothermal effect under the exclusive control of light, which in turn causes the coil-to-globule-transition of the polymer structure and the consequent hyperthermia-induced drug release. The choice of gold nanoparticles and PNM for the preparation of a GO–Au–PNM nanosystem was mainly driven by the high photothermal conversion efficiency of the plasmonic gold nanostructures in the visible region and the LCST behaviour of PNM. Furthermore, the easy preparation and chemical modification enable the AuNPs to be tailored in various ways to facilitate their integration into a variety of nanostructured materials. The GO–Au–PNM nanosystem was prepared and tested as depicted in Scheme 1. In detail, graphene was converted to GO nanosheets by Hummer's modified method. Then, the GO nanosheets were decorated with Au nanoparticles as described in the Experimental section. Finally, the linkage of

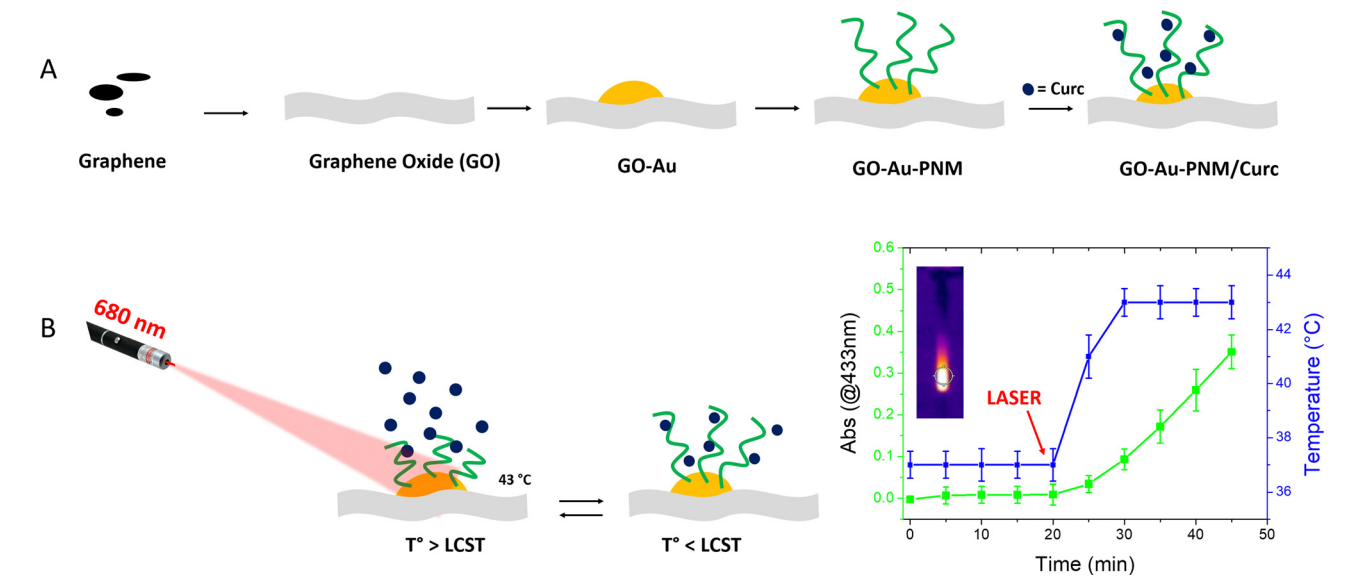

Scheme 1 Schematic illustration of (A) preparation of the GO–Au–PNM/Cur adduct; (B) laser irradiation of GO–Au–PNM/Cur (λ_{exc} 680 nm) for a combined photothermal and drug-release effect, the graph reports the increase of temperature (blue line) and curcumin photo-release as absorbance at 433 nm (green line) overtime.

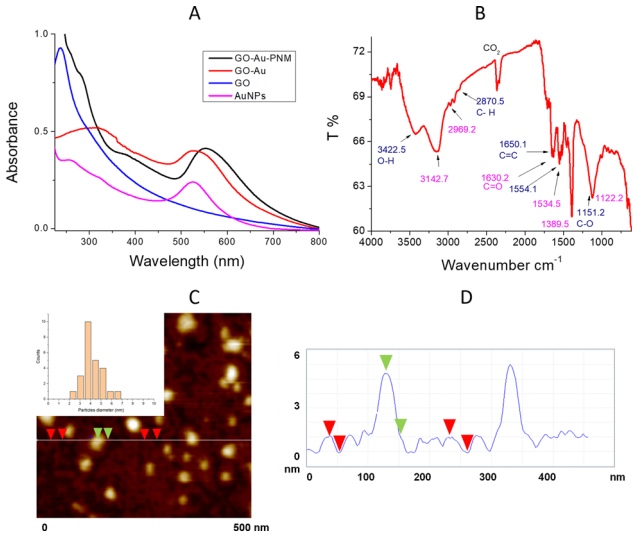

Fig. 1 Physicochemical characterization of GO–Au and GO–Au–PNM nanosystems: (A) optical absorption spectra of the dispersion of GO–Au–PNM, GO–Au, GO and AuNPs in water; (B) FTIR spectrum of GO–Au–PNM (cyan PNM and blue GO); (C) representative AFM images for GO–Au nanosystems on MICA substrate scan image 500 × 500 nm, (inset, size distribution for AuNPs); (D) cross sections for AuNPs.

PNM molecules with the Au nanoparticle surface was obtained exploiting the sulphur chemistry. The GO–Au–PNM nanosystem was fully characterized by various techniques. Fig. 1A illustrates the optical absorption spectra of an aqueous dispersion of GO–Au–PNM (black line). The LSPR broad band related to the Au nanoparticles at around 550 nm and the absorption in the region 230–280 nm related to the GO nanosheet were observed. For comparison, optical absorption spectra of AuNPs (cyan line) and GO sheet (blue line) alone were recorded. Notably, the LSPR band for the AuNPs in the GO–Au–PNM nanohybrid is broadened and red-shifted compared to that of GO–Au (red line) and AuNPs (cyan line). This finding not only corroborates the effective linkage of PNM to the AuNPs, but also indicates the electronic interactions between the two species, as reported for other species grafted to GO.[33] Moreover, as previously observed for similar Au nanostructured materials,[31] the red shifts of the AuNP LSPR band evidence both surface electronic interaction and nanoaggregation phenomena. The successful GO–Au formation was easily evidenced by the colour change of the GO suspension from brown-yellow to red-purple, which is consistent with the presence of the AuNPs. The further functionalization with thiolated PNM to produce GO–Au–PNM is evidenced by the red-shifted LSPR band in the GO–Au–PNM (Fig. 1A). The effective GO–Au–PNM formation was well supported by FTIR spectroscopy (Fig. 1B), showing the following diagnostic peaks for PNM: 3147.2 cm^{-1} (N–H, stretching), 2969.2 cm^{-1} (C–H, stretching), 1630.2 cm^{-1} (C═O stretching, amide I), 1534.5 cm^{-1} (C═O stretching, amide II), 1389.5 cm^{-1} (C–H, bending) and 1122.2 cm^{-1} (C–C, stretching). Moreover, the following FTIR peaks for GO sheets were recorded: 3422.5 cm^{-1} (O–H stretching), 2870.5 cm^{-1} (C–H stretching), 1650.1 cm^{-1} (C═C, stretching), 1554.1 cm^{-1} (CO, stretching) and 1151.2 cm^{-1} (C═O, bending). For comparison, FTIR-ATR spectra of the precursor GO-sheets and PNM were recorded (Fig. S1, ESI†). The morphology of the AuNPs on the GO sheets was investigated by contact-mode AFM. Fig. 1C shows representative scan 500 × 500 nm AFM images of the AuNPs. The investigation revealed the presence of spherical-shaped gold nanoparticles with a size ranging from 3 to 7 nm at the GO-sheet surface. The histogram distribution for the height size of AuNPs, obtained by analysis of different AFM images, is shown in the inset Fig. 1C. Fig. 1D shows the profile section of GO–AuNPs.

The comparison between the full scan 3 × 3 μm AFM images for GO–AuNPs and GO–Au–PNM revealed the effective GO–Au–PNM nanoaggregation, which is consistent with the red-shifted LSPR band observed for the GO–Au–PNM nanohybrid (Fig. 1A and Fig. S2, S3, ESI†).

The electronic structure of the GO–Au–PNM was investigated by X-ray photoelectron spectroscopy. This technique is ideal as it gives information on the oxidation states and on the chemical environment of the studied species and allows estimation of the surface elemental composition once the relevant atomic sensitivity factors have been considered.[34,35]

Fig. 2A shows the high-resolution XP spectrum of the functionalized GO–Au–PNM in the C 1s, O 1s, N 1s, S 2p and Au 4f energy regions. In detail, for the C 1s binding energy region, two signals are evident at 284.6 and a shoulder centred at 287.2 eV. The first component at 284.6 eV is due to the

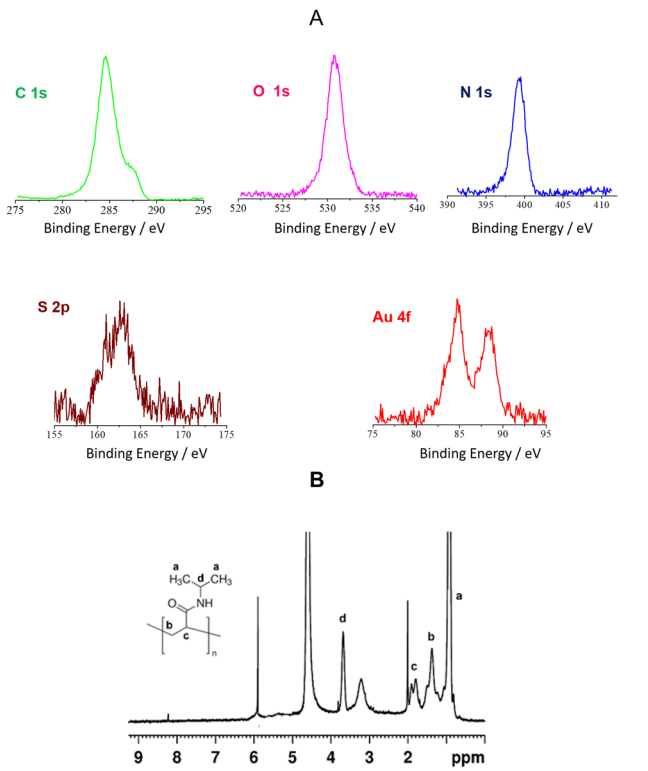

Fig. 2 GO–Au–PNM characterization: (A) Al Kα excited XPS in the C 1s, O 1s, N 1s, S 2p and Au 4f energy regions; (B) ^{1}H NMR spectrum of GO–Au–PNM (400.13 MHz, D_2O, 297 K).

aromatic and aliphatic backbones of the PNM functionalized graphene oxide. The components centred at 287.2 is due to the –C–OH and –C═O species of both GO and PNM.[36] Similarly, the O 1s binding energy region, consisting of a rather symmetrical peak at 530.7 eV, which is mainly due to the oxygen of the graphene oxide as well as the oxygen of the HN–C═O group of the PNM polymer.[36] The experimental profile of this N 1s signal shows just one peak at 399.3 eV, ascribed to the N atom of the HN–C═O group of the PNM polymer.[37–41] The high-resolution XP spectrum of the GO–Au–PNM in the S 2p binding energy region is rather noisy due to the low atomic concentration of S (0.4% of the overall XPS signals). Nevertheless, the peak centred at 162.5 eV, clearly shows the shape of the two expected 2p spin–orbit components and is due to the S of the functionalized PNM ligand. Finally, in the Au 4f binding energy region, the Au $4f_{7/2,5/2}$ levels were observed at 84.7 and 88.4 eV, respectively, and indicate the presence of Au^0 states. The XPS atomic concentration analysis of the investigated system clearly shows a ratio S/Au = 4.0, N/Au = 115, O/Au = 132, and N/S = 29.

The presence of the PNM pendants on the material surface was corroborated by the ^{1}H NMR spectrum of GO–Au–PNM (Fig. 2B). The proton spectrum showed peaks at 1.13 ppm (CH_3 of the isopropyl group), 1.57 ppm (CH_2– group on the backbone), 1.99 ppm (CH– group on the backbone) and 3.88 ppm (CH– group of the isopropyl),[41,42] which define the structure of the PNM polymer. The proton spectrum of GO–Au–PNM was very similar to the one of the PNM–polymer carbon dots that we reported in a previous paper.[29] Since the peaks belonging to the polymer normally are wider,[43] the best-defined peaks in the proton spectrum of GO–Au–PNM correspond to impurity, while the peak at 3.39 ppm, which is significantly smaller in the spectrum of pure PNM, could be due to possible isomeric structures. The peak at 8.22 ppm is attributable to residual NH proton that normally does not show up because it exchanges easily with D_2O. However, the fact that it shows up on the spectrum of the material but not in the spectrum of only PNM polymer can be related to the more rigid structure of the material that hinders the diffusion of water molecules toward the interior.

The effectiveness of GO functionalization was also corroborated by DLS and *Z*-potential measurements. The DLS investigation showed for GO dispersion in water is a main population of nanostructures with mean hydrodynamic diameters of 829.1 ± 75 nm (93%) and 194.1 ± 5 nm (7%). The further decoration with AuNPs, as expected, induces an increment of GO-nanosheet exfoliation and GO–Au nanostructures with a smaller diameter of 588.8 ± 23 nm (98.5%) were detected. Next, functionalization of the AuNPs with PNM causes an increase in the hydrodynamic size (674.8 ± 22 nm; 93%) due to the PNM chains (Fig. S4, ESI†). Aggregation of the GO–Au–PNM nanostructures (5098 ± 520 nm; 7%) was also observed according to the AFM data (Fig. S2 and S3, ESI†). *Z*-potential measurements showed a slight decrease in the GO *Z*-potential value (−55.4 ± 3.1 mV) upon AuNP decoration (GO–Au: −46.7 ± 1.4 mV). As expected, functionalization of the AuNPs with PNM to give the GO–Au–PNM nanohybrid further decreased the *Z*-potential value (−24.7 ± 0.9 mV). The PNM functionalization was also revealed by the typical LCST behaviour observed for the GO–Au–PNM, with a value of LCST above the human body temperature of 37 °C (Fig. S5, ESI†). The LCST value higher than that of a homogeneous solution of PNM (32–34 °C) was indicative of an effective interaction between PNM and Au nanoparticle surface as widely reported in the literature.[44–46] These data enable the use of PNM-based nanomaterials as drug-release systems at human body temperature.

With the aim to evaluate the potential of GO–Au–PNM as a light-responsive drug delivery system, we selected curcumin as a model of a hydrophobic drug and performed molecular dynamics simulations to investigate the Au–PNM/Cur interactions. In detail, five Au–PNM/Cur structures were randomly selected during the preliminary 10 ns of MD simulations, see the Methods section, respectively, at 298 K and 315 K (Fig. 3A and B). Results obtained at higher temperature revealed three structures with PNM collapsed chains at Au–NP surface (S01, S02 and S03) and two with PNM extended structures (S04 and S05). The energy difference for optimized geometries after conducting MD simulations reveals for the PNM collapsed structures (S01: 0.00 kcal mol^{-1}; S02: 5.52 kcal mol^{-1} and S03: 7.12 kcal mol^{-1}) lower energy values than the PNM extended structures (S04: 29.13 kcal mol^{-1} and S05: 32.43 kcal mol^{-1}). The main contribution to these values is mainly due to the Coulombic electrostatic interactions and van der Waals forces between PNM and Au nanoparticles.

These data indicate a strong interaction between PNM and the AuNP surface in agreement with the increase of the LCST values (above 37 °C) experimentally observed for the GO–Au–PNM nanostructures (Fig. 1A and Fig. S5, ESI†). Conversely, the results

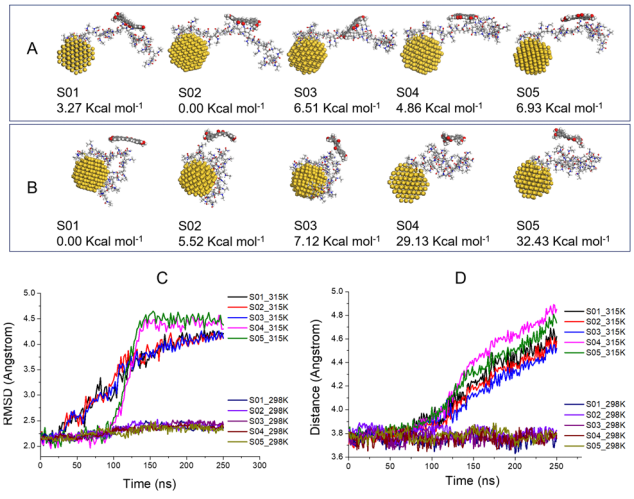

Fig. 3 Molecular dynamics simulations data for Au–PNM system: (A) snapshots of Au–PNM collapsed (S01, S02 and S03) and extended (S04 and S05) structures after 250 ns at temperature 315 K and (B) at 298 K (water molecules are omitted for clarity). The energy difference for all optimized structures has been reported: (C) RMSD for the five different geometries of Au–PNM/Cur at 315 K and 298 K; (D) time fluctuation of the average distance between Cur and Au nanoparticles surface for the five different geometries at 315 K and 298 K.

of MD simulations performed at 298 K indicate the exclusive presence of extended PNM structures, with minor differences in E_{int} observed among the five structures: (S01: 3.27 kcal mol^{-1}; S02: 0.00 kcal mol^{-1}; S03: 6.51 kcal mol^{-1}; S04: 4.86 kcal mol^{-1}; S05: 6.93 kcal mol^{-1}). No collapsed structure was revealed. The root mean square deviation (RMSD) values calculated within a timescale of 250 ns at 315 K confirm again the structure variation due to the LCST behaviour of PNM. The RMSD values increased by more than 2 Å during the simulation for all the structures investigated, a significant increase of the RMSD value from 2 Å to 4.5 Å within 50 ns, indicative of an effective LCST transition, was observed for the extended PNM structures (S04 and S05). Differently, the collapsed PNM structures (S01, S02 and S03) showed a slow increase of the RMSD values from 2.0 to 4.1 Å within 250 ns (Fig. 3C). All simulations revealed a reduced affinity of the curcumin molecules towards the Au–PNM nanoparticles at 315 K. Indeed, as depicted in Fig. 3D, at 315 K, the distance between curcumin and the Au nanoparticle surface increases within 250 ns indicating an effective release of drug from all the Au–PNM structures investigated. In contrast, RMSD values calculated at 298 K (Fig. 3C) exhibit a slight increase, suggesting that no polymer phase transition occurs at a temperature below LCST. Consequently, no significant structural differences have been revealed. In addition, a notable interaction between curcumin and the polymer chain occurs, as evidenced by the unaffected curcumin–PNM distance during the MD simulations, Fig. 3D.

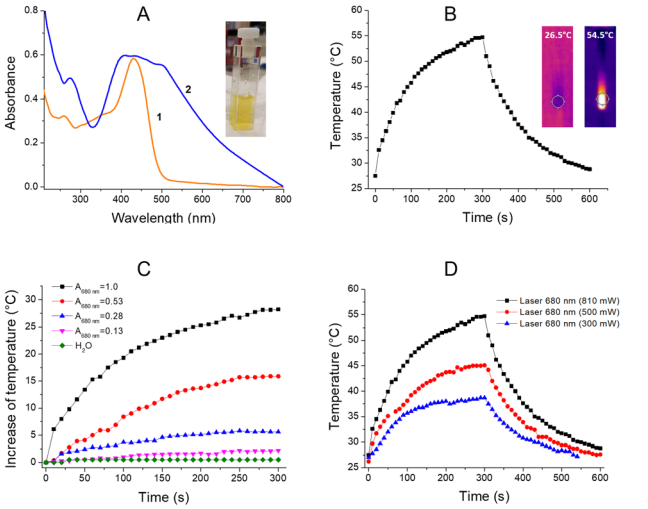

Fig. 4 GO–Au–PNM/Cur photothermal properties: (A) optical absorption spectra of Cur (line 1) in water/ethanol solution (70 : 30) and GO–Au–PNM/Cur (line 2) in water; representative photograph of GO–Au–PNM/Cur water dispersion (inset); (B) photothermal cycles for GO–Au–PNM/Cur, laser 680 nm (power 810 mW, volume 200 μL, Ass_{680nm} = 0.9); representative thermographs of GO–Au–PNM/Cur dispersion in water during the photothermal experiments (inset); (C) photothermal experiments for aqueous GO–Au–PNM at different absorbance value at 680 nm (laser power 810 mW); (D) photothermal effect of the GO–Au–PNM dispersion (200 μL, Abs_{680nm} = 0.9) at different laser power.

Curcumin loading and photothermal-induced release

To load Cur into the GO–Au–PNM, excess drug (3 : 1 w/w) was added to the GO–Au–PNM aqueous dispersion, and the mixture was stirred for 48 h. Then, the sample was dialyzed to remove the unentrapped drug. The formation of the GO–Au–PNM/Cur adduct was confirmed by spectroscopic methods and DLS measurements. The UV-Vis absorption spectrum of GO–Au–PNM/Cur (Fig. 4A) showed the Cur absorption band at 433 nm and the typical LSPR band of the AuNPs above 550 nm. To investigate the photothermal properties of the GO–Au–PNM, an aqueous dispersion (200 μL, Abs_{680nm} = 0.9) was continuously exposed to a 680 nm laser (810 mW power). The temperature changes were monitored using a thermal camera (Fig. 4B inset). When the temperature of the system reached the maximum value of about 54.5 °C (temperature difference = $T_{max} - T_{enviroment}$ = 28 °C), the laser was switched off and the temperature change during cooling was monitored. The cycles were repeated many times to confirm the reversible process; a representative photothermal cycle is depicted in Fig. 4B.

A photothermal conversion efficiency (η) value of about 16% was calculated. The photothermal time constants (τ_s) were calculated upon photoexcitation with 0.5 and 0.8 W laser power (680 nm, Fig. S6, ESI†). To better investigate the correlation between the photothermal activity and the absorbance at 680 nm, experiments were performed using GO–Au–PNM dispersions with different absorbance values. The results reported in Fig. 4C indicate temperature increases of about 2.3, 5.7, 15.9 and 28.5 °C for absorbance values (λ = 680 nm) of 0.13, 0.28, 0.53 and 1.0 unit, respectively. Moreover, the power-dependent behaviour was confirmed by experiments performed with different laser powers of 300, 500, and 810 mW, and the temperature difference values recorded were about 12.2, 18.6 and 28.3 °C, respectively (Fig. 4D). The photothermal properties of the GO–Au–PNM nanohybrid were also confirmed upon excitation with green-light 532 nm (Fig. S7, ESI†) and blue-light 405 nm (Fig. S8, ESI†) to show the photothermal versatility of the nanosystem.

To assess the combined photothermal and drug release effect of GO–Au–PNM/Cur, the dispersion was first incubated for 20 min at 37 °C under dark conditions and the absorbance measurements (at 433 nm) at various incubation times (0, 5, 10, and 20 min) were recorded. Under dark conditions, the absorbance spectra revealed a very slight Cur release (Fig. S9, ESI†). Then, a concurrent increase in temperature and absorbance signals were recorded upon few minutes of red-light irradiation (680 nm, 810 mW) indicative of an effective combined photothermal and drug release effect. Fig. 5A depicts the appearance of the optical absorption band for the released Cur at various irradiation time (0, 5, 10, 15, 20, and 25 min). Fig. 5B shows the combined increase of temperature (blue line) and the release of Cur (green line) overtime, with a drug release rate value of about 147 μg min^{-1} and a maximum temperature value of 42.5 °C.

In summary, as revealed by experimental data and supported by modelling simulation, the mechanism of the photothermal triggerable curcumin release is ascribable to the PNM conformational transition induced by the heat released from the Au–NPs upon red-light photoexcitation.

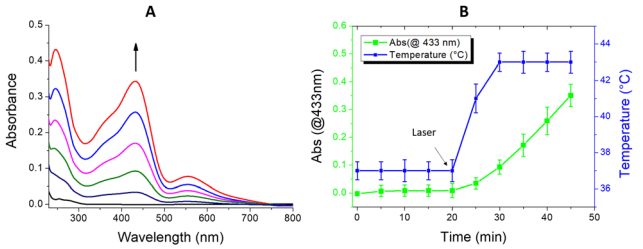

Fig. 5 GO–Au–PNM/Cur combined photothermal and drug release effect: (A) absorption band of the released Cur in water/ethanol solution (70 : 30) upon red-light laser exposition at different times (0, 5, 10, 15, 20, and 25 min); (B) combined photothermal and Cur release in the GO–Au–PNM/Cur dispersion (Ass_{680nm}= 0.18).

Cell viability and cellular uptake experiments

To evaluate the effect of the GO–Au–PNM nanohybrid on cell viability, human colorectal cells were exposed to increasing concentrations of GO–Au–PNM (0.004, 0.04, 0.4, and 4 μg μL^{-1}) for 24 h. As illustrated in Fig. 6A, at the end of the treatment and at any concentration used, the cell viability was comparable to that of untreated controls and no remarkable effects on cell morphology were observed after exposure to GO–Au–PNM (Fig. 6B and C). At the highest concentration, corresponding to 4 μg μL^{-1}, cell growth decrease was about 15.6% compared to the control (p value: 0.1079); at 0.4 μg μL^{-1}, the decrease was about 6.11% (p value: 0.8399); at 0.04 μg μL^{-1}, the difference was about 0.13% (p value: >0.9999), and finally at the lowest concentration of treatment, 0.004 μg μL^{-1}, the percentage difference between the control cells and the treated cells was about 3.07% (p value: 0.9846).

To evaluate the potential of GO–Au–PNM as a drug delivery system, cellular uptake experiments were performed on $CaCo_2$ cells. The confocal microscopy analysis (Fig. 6D) and laser scanning microscopy of untreated cells, used as control, showed no significant emission apart from the cell autofluorescence (Fig. 6E). Green staining was instead detected in the cells incubated with the GO–Au–PNM/Cur adduct. This finding evidenced that the luminescent GO–Au–PNM/Cur adducts penetrate the cell and accumulate in the cytoplasm.

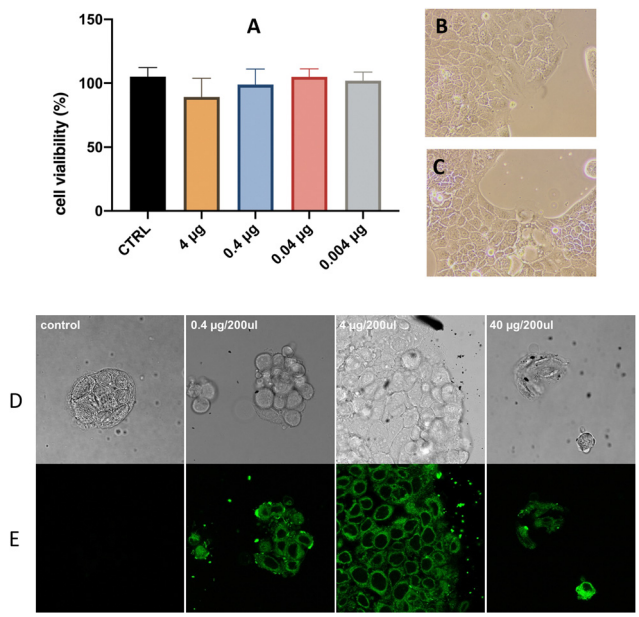

Fig. 6 Cell viability and internalization experiments: (A) MTT assays of human Colorectal ($CaCo_2$) cells treated for 24 h with increasing concentrations of GO–Au–PNM. Bars are means _ SEM of three independent experiments with n = 3; (B) representative photograph of cells CTRL; (C) representative photograph of cells with GO–Au–PNM (4 μg μL^{-1}); (D) representative optical microscopy micrographs; (E) laser scanning microscopy micrographs ($\lambda_{ex/em}$ = 405/500–600 nm) for $CaCo_2$ cells untreated (control) and treated with different GO–Au–PNM/Cur amount (0.4, 4.0, and 40 μg mL^{-1}).

Conclusions

A water-dispersible and photothermal-responsive three-component nanohybrid system composed of graphene oxide, gold nanoparticles and a PNM polymer was prepared and characterized for understanding the physicochemical and photothermal properties. The functionalization of the AuNPs anchored on graphene nanosheets with PNM provided a photothermal nanosystem potentially suitable for biomedical applications. Indeed, the GO–Au–PNM nanohybrid showed responsivity to a biocompatible and tissue-penetrating red-light stimulus, biocompatibility, and cellular uptake in human cell lines. The hybrid nanosystem loaded curcumin, selected as a hydrophobic drug model, and upon irradiation-triggered hyperthermia, released the drug by changing the PNM conformation as corroborated by molecular modelling. Microscopy fluorescence investigation confirmed that the GO–Au–PNM/Cur adduct can cross the cell membrane and reach the cytoplasm. The main innovation of the proposed nanohybrid system is the successful combination of good water dispersibility, red-light photoresponsivity, excellent biocompatibility and cellular uptake, drug loading capability and photothermal-controlled drug release. Despite stability and bioaccumulation being limitations, common to most hybrid nanosystems, and requiring further investigation, GO–Au–PNM is one of the first nanohybrid materials activable by a tissue-penetrating biofriendly red light that opens fascinating prospects in the research of novel powerful therapeutic tools based on synergistic chemo-photothermal effects.

Materials and methods

Chemicals

All chemicals were obtained from commercial sources in the highest possible purity and were used as received. Milli-Q-grade water was used in all preparations. All solvents used were of spectrophotometric grade.

Synthetic procedures

Preparation of GO–Au–PNM. GO was synthesized at room temperature using the simplified Hummers' method. To prepare the GO–Au product, a GO aqueous suspension (40 mL, 2 mg mL^{-1})

was bath sonicated for 1 h to give a clear solution then an aliquot of 75 μL of $HAuCl_4$ (5×10^{-2} M) was added. After 10 minutes of stirring at 70 °C ± 2 °C, an aliquot of sodium citrate was added (10 mg mL^{-1}). After one hour of reaction, the red-purple dispersion of GO–Au was centrifuged at 2000 rpm for 10 min to separate the GO–Aus from unreacted reagents and AuNPs. The resulting GO–Au dispersion was purified by dialysis for 24 hours, using a 3.5–5 KDa cut-off dialysis membrane and MilliQ-water. Finally, the GO–Au–PNM was prepared by reaction of the GO–Au dispersion (5 mL, 2 mg mL^{-1}) with PNM-thiolated (1 mM) at room temperature for 24 hours. The resulting dispersion was purified by dialysis using MilliQ-water through a dialysis membrane (3.5–5 KDa cut off) for 46 hours.

Preparation of GO–Au–PNM/Cur. GO–Au–PNM/Cur was prepared by adding an excess of Cur (1 : 3 w/w) to the GO–Au–PNM colloidal solution (10 mL), and the mixture was stirred for 48 h at room temperature. Then, the sample was dialyzed for 24 h using MilliQ-water–ethanol medium (70 : 30) through a dialysis membrane (3.5–5 KDa cut off) to remove the unentrapped drug.

X-ray photoelectron spectroscopy (XPS) measurements. XPS investigation of the freshly prepared samples, deposited on Si substrates, were performed at 45° relative to the sample stage plane with a PHI 5600 multi technique system (base pressure of the main chamber 1×10^{-8} Pa). Spectra were excited with monochromatized Al-Kα radiation. The pass energy was set to 11.85 eV. XPS peak intensities were obtained after Shirley's background removal. Spectral calibration was achieved by fixing the Au $4f_{7/2}$ peak of a clean Au sample at 84.0 eV. This method turned the main C 1s peak at 284.6 eV. No charging effect during the XPS analyses was observed since the GOAuSPNM material was on silicon, and the molybdenum sample holder was conducting. Experimental uncertainties in binding energies lie within ±0.4 eV. The surface atomic concentration of the samples was calculated considering the relevant atomic sensitivity factors.

Photothermal properties of GO–Au–PNM. The photothermal properties of GO–Au–PNM were investigated by irradiating a glass tube (diameter 3 mm) containing various amounts of the GO–Au–PNM dispersion. A volume of 100 μL of the GO–Au–PNM dispersion was irradiated with a CW laser of 680 nm at various laser powers for various minutes. We used a FLIR infrared thermal imaging camera to measure the temperature of the solution every 10 s, during the heating and cooling process.

Photothermal release of Cur. To assess the photothermally triggered release of Cur, from the GO–Au–PNM/Cur nanohybrid, aliquots of 600 μL were dispensed on a micromembrane for dialysis (cutoff 3.5–5 kDa) and dipped in 1.7 mL of water–ethanolic (70 : 30) in a standard quartz spectroscopic cuvette. The solution was maintained under stirring during all experiments. The GO–Au–PNM/Cur was exposed to the laser source (680 nm) and the temperature of the GO–Au–PNM/Cur dispersion was measured using a thermal camera. The amount of Cur released was spectrophotometrically measured after each laser exposition.

Modelling simulation. The model investigated was built as follows: the Au unit cell replicated in the three spatial directions, obtaining a supercell from which a spherical gold nanoparticle with a diameter of 3.0 nm was generated using the build nanostructure tools included in the Material Studio 2017 package. Subsequently, a chain of 40-mer PNM was built using CHARMM-GUI[45] and covalently bonded to the nanoparticle *via* a sulphur atom. Additionally, a curcumin molecule was physiosorbed onto the polymer structure. The selected polymer length is considered optimal for studying the polymer phase transition.[46] The resulting system was placed in the center of a box measuring 5 × 9 × 9 nm (Fig. S10, ESI†), solvated with water molecules, and equilibrated using a procedure involving 25.000 steps of minimization with the steepest descent algorithm, followed by a 10 ns MD simulation at 298 K. In this timescale, five structures were randomly sampled and used as starting configurations for 250 ns MD simulations, with atomic coordinates saved every 1.0 ns for subsequent analysis. All the simulations were conducted under periodic boundary condition using the Forcite package included in the Material studio 2017 software.[47] The polymer consistent force field (PCFF) was employed, along with the PCFF water model, whose application has demonstrated good agreement with experimental data.[48] The *NPT* ensemble was selected for the simulations, the pressure was set to 1 atm and controlled by the Berendsen barostat (decay constant set to 0.1 ps) while the temperature was maintained respectively at 298 K, below the LCST, and 315 K, above the LCST, using the Nose thermostat (Q ratio = 0.01). A time step of 1 fs was set to integrate the equation of motion. For calculating long-range electrostatic interactions, the Ewald summation method was employed, with a cut-off distance of 1.0 nm, the charge equilibration method was chosen to evaluate the atomic charges. Additionally, Na^+ counterions were included to maintain the electric neutrality condition, given that curcumin was considered doubly negatively charged. The root means square deviations, RMSDs, of the generated trajectories, compared to the initial structure were computed as follows:

$$\mathrm{RMSD}(t) = \sqrt{\frac{1}{N}\sum_{k=1}^{N}\left(r_k(t) - r_k^{\mathrm{init}}\right)^2}$$

where N is the total number of atoms, $r_k(t)$ are the instantaneous coordinates of atom k and r_k^{init} are the initial coordinates of atom k where N in the total number of atoms, $r_k(t)$ are the instantaneous coordinates of atom k and r_k^{init} are the initial coordinates of atom k. For each of the five structures, the interaction energy between AuNP–PNM and curcumin is calculated by optimizing the structure obtained after conducting MD simulations, as

$$E_{\mathrm{int}} = E_{\mathrm{AuNP-PNM-Cur-water}} - \left(E_{\mathrm{AuNP-PNM}} + E_{\mathrm{water}} + E_{\mathrm{Cur}}\right)$$

The total energy comprises contributions from bonded energy terms, out-of-plane energy, cross-interaction terms, Coulombic electrostatic interactions, and the van der Waals force.

Cell culture for internalization test. CaCo-2 cells [ATCC HTB-3] were maintained in DMEM with addition of 10% fetal bovine

serum (Sigma-Aldrich F9665) and 1% penicillin/streptomycin (Sigma-Aldrich P4333) and incubated at 37 °C and 5% CO_2 CaCo-2 cells were seeded at appropriate cell-concentration in 8-well μ-slide glass bottom 1.5H (170 μm ± 5 μm) D 263 M Schott glass, sterilized (Ibidi, Cat. No. 80827) and let them grow for 24 h. GO–Au–PNM/Cur was added to the cell-culture medium (volume per well 200 μL) in increasing amounts from 0.4 μg to 40 μg per well, and left incubating for 24 h. After incubation, the cells were washed once with fresh medium, to remove the nanosystem excess in the extracellular medium. Then, the cells were imaged.

Fluorescence image acquisition. Images were acquired on a confocal microscope, Leica TCS SP8, using an HCX PL APO CS2 63× 1.40 NA oil immersion objective lens (Leica Microsystems, Mannheim, Germany). The microscope is equipped with an incubation chamber to keep the cells at 37 °C and 5% CO_2. The pinhole size was set to 1 Airy Unit. 1024 × 1024-pixel images were acquired with a pixel size of 140 nm. Fluorescent GO–Au–PNM/Cur was excited at 405 nm and the fluorescence emission was detected in the band 500–600 nm using a photomultiplier tube. The transmitted light detector (TLD) channel was used to visualize the morphology of the cells.

Cell viability test. To evaluate the effect of GO–Au–PNM nanostructures on human colorectal adenocarcinoma cells, an MTT ([3-(4,5-dimethylthiazol-2-yl)-2,5-diphenyltetrazolium bromide]) assay was performed. Briefly, human colorectal adenocarcinoma cells (CaCo-2 HTB-37TM, American Type Culture Collection, Manassas, VA, USA) were grown in Dulbecco's MEM (DMEM) with 10% heat-inactivated fetal bovine serum, 2 mM L-alanyl-L-glutamine, penicillin–streptomycin (50 units–50 μg for mL) and incubated at 37 °C in a humidified atmosphere of 5% CO2, 95% air. CaCo-2 cells were plated in 96 well plates and incubated at 37 °C. A GO–Au–PNM stock solution (40 μL, 0.1 mg μL^{-1}) was prepared in nuclease free water. A series of dilutions were performed to obtain different GO–Au–PNM concentrations (1 μg μL^{-1}, 100 ng μL^{-1} and 10 ng μL^{-1} and 1 ng μL^{-1}). Cells were treated with 40 μL of each solution. 5-Fluoroacil (Ref. F6627, Merck KgaA, Darmstadt, Germany) was prepared as a 1 mM solution in 10 mL with 0.01% DMSO and tested at arbitrary concentrations of 100 μM, 10 μM, 1 μM, 0.1 μM and 0.01 μM. Untreated cells were used as controls. Microplates were incubated at 37 °C in a humidified atmosphere of 5% CO_2, 95% air for 24 h, and then, cytotoxicity was measured with colorimetric assay based on the use of tetrazolium salt MTT (3-(4,5-dimethylthiazol-2-yl)-2,5-diphenyl tetrazolium bromide). The results were read on a multiwell scanning spectrophotometer (H1 Synergy plate reader, Biotech, Milan, Italy), at a wavelength of 569 nm. Each value was an average of 8 wells. The percentage difference from the untreated cells for the nanoparticles was calculated using the GraphPad Prism 6.0 software. IC50 expresses the concentration of the tested compound necessary to kill half of the cell population after 24 h of incubation relative to untreated controls.

Instrumentation. UV-Vis spectra were recorded on a PerkinElmer 365 spectrophotometer using quartz cells with a path length of 1 cm and 0.1 cm. FTIR spectra were recorded on a PerkinElmer spectrophotometer. The particle size and surface charge were examined by using a combined dynamic light scattering and zeta-potential apparatus ZetaSizer NanoZS90 (Malvern Instrument, Malvern, UK) equipped with a 633 nm laser, at the scattering angle of 90° and 25 °C temperature. AFM measurements were carried out in soft tapping mode in air using a Bruker FAST-SCAN microscope. The probes used were Fast-Scan A, with a nominal tip radius of 5 nm, a spring constant of 18 N m^{-1}, and a resonance frequency of 1.400 KHz. An aliquot of GO–Au–PNM dispersion was deposited on a fresh mica substrate and then dried under vacuum (10 mbar). Each sample was typically characterized by acquiring five images obtained at different points. NMR spectra were recorded on a Bruker 400™ spectrometer. GO–Au–PNM sample, previously freeze-dried, was dissolved in deuterated water (D_2O) and analyzed at 297 K.

Author contributions

The manuscript was written with the contributions from all authors. All authors have given approval for the final version of the manuscript.

Conflicts of interest

There are no conflicts to declare.

Acknowledgements

This work has been funded by European Union (NextGeneration EU), through the MUR-PNRR project SAMOTHRACE (ECS00000022) and by MUR ex D.M.n.1059 del 09/08/2021 (CUP: E93C22003310001) Project title: L'innovazione delle Biotecnologie nell'Era della Medicina di Precisione, dei Cambiamenti climatici e dell'Economia Circolare.

References

1 N. Zhao, L. Yan, X. Zhao, X. Chen, A. Li, D. Zheng, X. Zhou, X. Dai and F.-J. Xu, Versatile Types of Organic/Inorganic Nanohybrids: From Strategic Design to Biomedical Applications, *Chem. Rev.*, 2019, **119**(3), 1666–1762.
2 X. Xue, H. Qu and Y. Li, Stimuli-responsive crosslinked nanomedicine for cancer treatment, *Exploration*, 2022, **2**, 20210134.
3 J. Chen, J. Yang and J. Ding, Rational construction of polycystine-based nanoparticles for biomedical applications, *J. Mater. Chem. B*, 2022, **10**, 7173–7182.
4 J. Chen, Z. Jiang, Y. S. Zhang, J. Ding and X. Chen, Smart transformable nanoparticles for enhanced tumor theranostics, *Appl. Phys. Rev.*, 2021, **8**, 041321.
5 A. Joy, G. Unnikrishnan, M. Megha, M. Haris, J. Thomas, E. Kolanthai and S. Muthuswamy, Design of biocompatible polycaprolactone-based nanocomposite loaded with graphene

oxide/strontium nanohybrid for biomedical applications, *Appl. Nanosci.*, 2023, **13**, 4471–4484.
6 Q. Li, H. He, S. Wang, H. Zhai, Y. Shen, A. Li and F. Guan, Bis(2-hydroxyethyl) Terephthalate-Modified $Ti_3C_2T_x$/Graphene Nanohybrids as Three-Dimensional Functional Chain Extenders for Polyurethane Composite Films with Strain-Sensing and Conductive Properties, *ACS Appl. Mater. Interfaces*, 2023, **15**, 12403–12413.
7 S. Lanzalaco, J. Mingot, J. Torras, C. Alemán and E. Armelin, Recent Advances in Poly(*N*-isopropylacrylamide) Hydrogelsand Derivatives as Promising Materials for Biomedical and Engineering Emerging Applications, *Adv. Eng. Mater.*, 2023, **25**, 2201303.
8 B. Joe, M. Vijaykumar and B. R. Lokesh, Biological Properties of Curcumin-Cellular and Molecular Mechanisms of Action, *Crit. Rev. Food Sci. Nutr.*, 2004, **44**, 97–111.
9 C. Porro and M. A. Panaro, Recent Progress in Understanding the Health Benefits of Curcumin, *Molecules*, 2023, **28**, 2418.
10 S.-I. Sohn, A. Priya, B. Balasubramaniam, P. Muthuramalingam, C. Sivasankar, A. Selvaraj, A. Valliammai, R. Jothi and S. Pandian, Biomedical Applications and Bioavailability of Curcumin—An Updated Overview, *Pharmaceutics*, 2021, **13**, 2102.
11 C. de Waure, C. Bertola, G. Baccarini, M. Chiavarini and C. Mancuso, Exploring the Contribution of Curcumin to Cancer Therapy: A Systematic Review of Randomized Controlled Trials, *Pharmaceutics*, 2023, **15**, 1275.
12 H. J. Denison, S. L. Schwikkard, M. Khoder and A. F. Kelly, Review: The Chemistry, Toxicity and Antibacterial Activity of Curcumin and Its Analogues, *Planta Med.*, 2023, DOI: **10.1055/a-2157-8913**.
13 M. J. Dehzad, H. Ghalandar, M. Nouri and M. Askarpour, Antioxidant and anti-inflammatory effects of curcumin/turmeric supplementation in adults: A GRADE-assessed systematic review and dose-response meta-analysis of randomized controlled trials, *Cytokine*, 2023, **164**, 156144.
14 S. Kaushik, N. Masand, M. R. Iyer and V. M. Patil, Preclinical to Clinical profile of Curcuma longa as Antidiabetic Therapeutics, *Curr. Top. Med. Chem.*, 2023, **23**, 2267–2276, DOI: **10.2174/1568026623666230428101440**.
15 S. Abolfazli, A. E. Butler, T. Jamialahmadi and A. Sahebkar, A Golden Shield: The Protective Role of Curcumin Against Liver Fibrosis, *Curr. Med. Chem.*, 2023, **31**, DOI: **10.2174/0929867331666230821095329**.
16 S. Heidari, S. Mahdiani, M. Hashemi and F. Kalalinia, Recent advances in neurogenic and neuroprotective effects of curcumin through the induction of neural stem cells, *Biotechnol. Appl. Biochem.*, 2020, **67**, 430–441.
17 N. A. Torbat, I. Akbarzadeh, N. Rezaei, Z. Moghaddam, S. Bazzazan and E. Mostafavi, Curcumin-Incorporated Biomaterials: In silico and in vitro evaluation of biological potentials, *Coord. Chem. Rev.*, 2023, **492**, 215233.
18 G. Granata, I. Paterniti, C. Geraci, F. Cunsolo, E. Esposito, M. Cordaro, A. R. Blanco, S. Cuzzocrea and G. M. L. Consoli, Potential Eye Drop based on a Calix[4]arene Nanoassembly for Curcumin Delivery: Enhanced Drug Solubility, Stability and Anti-Inflammatory Effect, *Mol. Pharm.*, 2017, **14**, 1610–1622.
19 G. Granata, S. Petralia, G. Forte, S. Conoci and G. M. L. Consoli, Injectable supramolecular nanohydrogel from a micellar self-assembling calix[4]arene derivative and curcumin for a sustained drug release, *Mater. Sci. Eng., C*, 2020, **111**, 110842.
20 V. S. Madamsetty, M. Vazifehdoost, S. H. Alhashemi, H. Davoudi, A. Zarrabi, A. Dehshahri, H. S. Fekri, R. Mohammadinejad and V. K. Thakur, Next-Generation Hydrogels as Biomaterials for Biomedical Applications: Exploring the Role of Curcumin, *ACS Omega*, 2023, **8**, 8960–8976.
21 J.-C. Tang, H.-S. Shi, L.-Q. Wan, Y.-S. Wang and Y.-Q. Wei, Enhanced antitumor effect of curcumin liposomes with local hyperthermia in the LL/2 model, *Asian Pac. J. Cancer Prev.*, 2013, **14**(4), 2307–2310.
22 Y. Tian, D. Jia, M. Dirican, M. Cui, D. Fang, C. Yan, J. Xie, Y. Liu, C. Li, J. Fu, H. Liu, G. Chen, X. Zhang and J. Tao, Highly Soluble and Stable, High Release Rate Nanocellulose Codrug Delivery System of Curcumin and AuNPs for Dual Chemo-Photothermal Therapy, *Biomacromolecules*, 2022, **23**(3), 960–971.
23 M. N. I. Amir, A. Halilu, N. M. Julkapli and A. Ma'amor, Gold-graphene oxide nanohybrids: A review on their chemical catalysis, *J. Ind. Eng. Chem.*, 2020, **83**, 1–13.
24 P. Majumdera and R. Gangopadhyay, Evolution of graphene oxide (GO)-based nanohybrid materials with diverse compositions: an overview, *RSC Adv.*, 2022, **12**, 5686–5719.
25 E. A. Asl, M. Pooresmaeil and H. Namazi, Chitosan coated MOF/GO nanohybrid as a co-anticancer drug delivery vehicle: Synthesis, characterization, and drug delivery application, *Mat. Chem. Phys.*, 2023, **293**, 126933.
26 N. Marino, S. Petralia, M. Perez-Loret, J. Mosinger, S. Conoci and S. Sortino, Graphene oxide nanohybrid photoreleasing nitric oxide, *J. Mat. Chem. B*, 2016, **4**, 5763–5948.
27 S. Mohammadi, A. Babaei and Z. Arab-Bafrani, Polyethylene Glycol-decorated GO Nanosheets as a Well-Organized Nanohybrid to Enhance the Performance of Chitosan Biopolymer, *J. Polym. Environ.*, 2022, **30**, 5130–5147.
28 S. Kakkar, S. Chauhan Bharti, M. Rohit and V. Bhalla, Conformational switching of aptamer biointerfacing graphene-gold nanohybrid for ultrasensitive label-free sensing of cardiac Troponin I, *Bioelectrochemistry*, 2023, **150**, 108348.
29 G. M. L. Consoli, M. L. Giuffrida, C. Satriano, T. Musumeci, G. Forte and S. Petralia, A novel facile one-pot synthesis of photothermally responsive carbon polymer dots as promising drug nanocarriers, *Chem. Commun.*, 2022, **58**, 3126–3129.
30 G. Forte, G. Consiglio, C. Satriano, L. Maugeri and S. Petralia, A nanosized photothermal responsive core-shell carbonized polymer dots based on poly(N-isopropylacrylamide) for light-triggered drug release, *Colloids Surf., B*, 2022, **217**, 112628.
31 G. M. L. Consoli, G. Forte, L. Maugeri, V. Consoli, V. Sorrenti, L. Vanella, G. Buscarino, S. Agnello, M. Camarda, G. Granata, L. Ferreri and S. Petralia, Near-Infrared-

Responsive Choline-Calix[4]arene-Gold Nanostructures for Potential Photothermal Cancer Treatment, *ACS Appl. Nano Mater.*, 2023, **6**, 358–369.

32 G. M. L. Consoli, M. L. Giuffrida, S. Zimbone, L. Ferreri, L. Maugeri, M. Palmieri, C. Satriano, G. Forte and S. Petralia, Green Light-Triggerable Chemo-Photothermal Activity of Cytarabine-Loaded Polymer Carbon Dots: Mechanism and Preliminary In Vitro Evaluation, *ACS Appl. Mater. Interfaces*, 2023, **15**, 5732–5743.

33 N. Karousis, A. S. D. Sandanayaka, T. Hasobe, S. P. Economopoulos, E. Sarantopoulou and N. Tagmatarchis, Graphene oxide with covalently linked porphyrin antennae: Synthesis, characterization and photophysical properties, *J. Mater. Chem.*, 2011, **21**, 109–117.

34 A. Gulino, Structural and Electronic Characterization of Self-Assembled Molecular Nanoarchitectures by X-ray Photoelectron Spectroscopy, *Anal. Bioanal. Chem.*, 2013, **405**, 1479–1495.

35 A. Gulino, G. G. Condorelli, P. Mineo and I. Fragalà, An x-ray photoelectron spectra and atomic force microscopy characterization of silica substrates engineered with a covalently assembled siloxane monolayer, *Nanotechnology*, 2005, **16**, 2170.

36 H. Ding, S. B. Yu, J. S. Wei and H. M. Xiong, Full-Color Light-Emitting Carbon Dots with a Surface-State-Controlled Luminescence Mechanism, *ACS Nano*, 2016, **10**, 484–491.

37 L. Motiei, M. Altman, T. Gupta, F. Lupo, A. Gulino, G. Evmenenko, P. Dutta and M. E. Van der Boom, Self-Propagating assembly of a molecular-based multilayer, *J. Am. Chem. Soc.*, 2008, **130**, 8913–8915.

38 A. Contino, G. Maccarrone, M. E. Fragalà, L. Spitaleri and A. Gulino, Gold–Porphyrin Monolayers Assembled on Inorganic Surfaces, *Chem. – Eur. J.*, 2017, **23**, 14937–14943.

39 J. Choudhury, R. Kaminker, L. Motiei, G. de Ruiter, M. Morozov, F. Lupo, A. Gulino and M. E. Van der Boom, Linear *vs*. Exponential Formation of Molecular-Based Assemblies, *J. Am. Chem. Soc.*, 2010, **132**, 9295–9297.

40 L. Spitaleri, G. Nicotra, M. Zimbone, A. Contino, G. Maccarrone Alberti and A. Gulino, Fast and Efficient Sun Light Photocatalytic activity of Au_ZnO Core-Shell Nanoparticles Prepared by a One Pot Synthesis, *ACS Omega*, 2019, **4**, 15061–15066.

41 M. V. Deshmukh, A. A. Vaidya, M. G. Kulkarni, P. R. Rajamohanan and S. Ganapathy, LCST in poly(*N*-isopropylacrylamide) copolymers: high resolution proton NMR investigations, *Polymer*, 2000, **41**, 7951–7960.

42 L. Starovoytova, J. Spevaceka and M. Ilavsky, 1H-NMR study of temperature-induced phase transitions in D_2O solutions of poly(N-isopropylmethacrylamide)poly(*N*-isopropylacrylamide) mixtures and random copolymers, *Polymer*, 2005, **46**, 677–683.

43 R. A. Stile, W. R. Burghardt and K. E. Healy, Synthesis and characterization of injectable poly(*N*-isopropylacrylamide)-based hydrogels that support tissue formation in vitro, *Macromolecules*, 1999, **32**, 7370–7379.

44 N. M. Huang, N. H. Lim, C. H. Chia, M. A. Yarmo and M. R. Muhamad, Simple room-temperature preparation of high-yield large-area graphene oxide, *Int. J. Nanomed.*, 2011, **6**, 3443–3448.

45 S. Jo, T. Kim, V. G. Iyer and W. Im, CHARMM-GUI: A Web-based Graphical User Interface for CHARMM, *J. Comput. Chem.*, 2008, **29**, 1859–1865.

46 G. Consiglio and G. Forte, Molecular dynamics study of coil-to-globule transition in a thermos-responsive oligomer bound to various surfaces: hydrophilic surfaces stabilize the coil form, *Phys. Chem. Chem. Phys.*, 2018, **20**, 29754–29763.

47 Material Studio package, BIOVIA, Dassault Systemes, San Diego, USA, 2017.

48 G. Consiglio, S. Failla, C. G. Fortuna, L. D'Urso and G. Forte, Aggregation of a Zn(II)-salen complex: Theoretical study of structure and spectra, *Comput. Theor. Chem.*, 2015, **1067**, 1–6.